# Constituent Phase Distribution in Ni-base Superalloy Brazes: Boron-Suppressed Versus Multi Principal Element Alloy Foils

Benjamin Schneiderman <sup>1, 2</sup>, Aric Adamson <sup>1</sup>, Warren Miglietti <sup>3</sup>, Zhenzhen Yu <sup>1, 2</sup>

<sup>1</sup> Colorado School of Mines, Golden, CO, USA

<sup>2</sup> HYSA Fillers LLC, Golden, CO USA

<sup>3</sup> Prince and Izant Co., Cleveland, OH, USA

#### **Abstract**

In this study, two different boron-suppressed brazing fillers (MBF80 and MBF91) and one MnFeCoNiCu-type multiprincipal element alloy (MPEA) filler were evaluated for their impact on the local constituent phase distribution in brazes of Inconel 738LC. Brazing was performed at 1200°C for 90 min using 60 µm total foil thickness, followed by the standard dualage heat treatment (2h at 1121°C / 24h at 843°C) to reprecipitate a bimodal distribution of  $\gamma$ ' in the base material. The boron-suppressed fillers MBF80 and MBF91 both introduced Cr-rich borides in both standalone (blocky) and lamellar morphologies typically around 20 um. No secondary phases foreign to the base material were observed in the MPEA braze, but MC and M<sub>23</sub>C<sub>6</sub> carbides typically found in the base material were present, with the M<sub>23</sub>C<sub>6</sub> at the braze centerline grain boundaries. All three brazes displayed appreciable  $\gamma$ ' precipitation throughout their transverse profile despite none of the original fillers containing the  $\gamma$ '-forming elements Al and Ti, indicating substantial introduction of these elements from the base alloy. The  $\gamma$ ' volume fraction was about 40% in the base material. After brazing and dual-age heat treatment, the braze centerlines exhibited about 56% γ' in MBF91 filler, 40% in MBF80, and approximately 27% in MPEA. The increase in MBF91 γ' fraction was attributed to the high Nb content of this filler, as Nb stabilizes the precipitate, while the  $\gamma$ ' decrease in the MPEA braze was attributed to the MPEA constituents locally diluting the introduced Al and Ti. Additionally, the  $\gamma$ ' size distribution in the MPEA was unimodal rather than bimodal, due to a local suppression of the solvus temperature causing y' to remain in solution during the first age heat treatment step at 1121°C. Both the MBF80 and MBF91 brazes exhibited widely nonuniform and elevated microhardness near the centerline due to indents contacting interspersed boride particles, while the MPEA braze exhibited a mild microhardness decrease due to the lower γ' volume fraction.

## Introduction

Nickel base superalloys are distinguished by their ability to retain excellent mechanical properties and corrosion resistance at high fractions of their melting temperature, making them suitable for high temperature applications such as hot-section components of gas turbine engines. Gamma-prime ( $\gamma$ ') precipitate-strengthened Ni-base superalloys are often employed in the most demanding operating environments, invoking the high solvus temperature (typically 1120-1170°C) of this coherent L1<sub>2</sub> precipitate to effectuate their high

temperature strength [1, 2]. Generally, alloy fabricability and weldability decrease with increasing concentration of Al and Ti, the major  $\gamma$ '-forming elements [3]. Inconel 738LC (IN738LC) is an archetypal  $\gamma$ '-strengthened alloy with 3.4 wt. % each of Al and Ti [4], and an optimal  $\gamma$ ' volume fraction of about 40% after standard heat treatments [2]. As such, microfissuring often plagues the heat affected zone of IN738LC welds [5, 6], with at least one study directly attributing this cracking to constitutional liquation of the  $\gamma$ ' [7].

As a result of the limitations in weldability, brazing is often employed as an alternative assembly and repair technique for  $\gamma$ '-strengthened superalloys, with IN738LC among the most frequently selected Ni-base materials for brazing studies [8]. Since the 1970s, the predominant strategy for brazing alloys like IN738LC has been transient liquid phase (TLP) bonding with a boron- and/or silicon-suppressed brazing filler [9]. Ideally, this process effectuates a braze that is microstructurally homogeneous with the parent material. This is accomplished through complete isothermal solidification driven by the diffusion of boron and/or silicon into the base material, causing a progressive rise in the filler melting point. To effectuate wider-gap brazes, particles of the base material in powder form are often added as additional diffusion sinks [8]. In practice, insufficient isothermal holding time, or deviations from ideal equilibrium and maximum solubility at the solid-liquid interface, frequently introduce either athermally-solidified or diffusion-induced boride and/or silicide phases to the braze [9, 10]. These phases are brittle and degrade the braze properties relative to the parent material, especially ductility to less than

An emerging strategy for brazing Ni-base superalloys is the use of multi-principal element alloy (MPEA) fillers designed to have an appropriate melting point without the addition of boron or silicon, and to resist the formation of intermetallic compounds through their high configurational entropy. Independent research studies have explored CoCrCuFeNiGa [11] and NiCrFeGe [12] alloy systems as candidates for MPEA braze fillers, while the authors' research group has focused primarily on the MnFeCoNiCu alloy system [13-15]. As described in detail in [14], the solidification mechanism for a MnFeCoNiCu-type alloy is single-phase, rendering complete isothermal solidification unnecessary to avoid secondary phase formation. In trial brazes of Inconel 600, the absence of borides or other intermetallic phases when using this MPEA filler led to a tenfold increase in the total elongation of tensile specimens incorporating the braze, relative to a braze performed with a boron- and silicon-suppressed filler [14].

Laser welds made between the MnFeCoNiCu-type MPEA and IN738LC indicated no immediate intermetallic phase formation [16], despite the greater number of alloying additions in IN738LC relative to Inconel 600.

A thorough assessment of the constituent phase distribution is critical to predict and understand performance of superalloy brazes. Most existing studies on constituent phases focus primarily on the distribution of borides in the case of boronsuppressed fillers (e.g., [17, 18]), or other multi-micron scale secondary phases in the case of boron-free variants [19] or MPEAs [11, 12]. Despite the role of submicron  $\gamma$ ' as the major strengthening phase of IN738LC and similar alloys, there is relatively little information available pertaining to the local impact of boron- and/or silicon-suppressed brazes on the  $\gamma$ ' distribution, and there is no prior work in understanding the effects of an MPEA braze on  $\gamma$ '. It is noteworthy that many of the most common boron- and/or silicon-suppressed fillers [20], as well as the aforementioned MPEA systems, contain no Al or Ti in the filler material alone. An important consideration when evaluating the braze impact on  $\gamma$ ' is that for any filler-substrate pair, a degree of substrate dissolution will occur at brazing temperatures above the filler liquidus, promoting material intermixing in the liquid state early in the brazing process [9]. This phenomenon, along with subsequent solid-state interdiffusion, may therefore introduce  $\gamma$ '-forming elements from the base material into the braze region, but the extent to which y' forms has not been quantified. This paper aims to alleviate some of these knowledge gaps by assessing the impact of two boron-suppressed brazing fillers and the MnFeCoNiCutype MPEA filler on the local constituent phase distribution, including y' precipitates. Microstructural comparisons are drawn among the three fillers, and the impact of each on the braze microhardness profile is discussed.

## **Experimental Methods**

## **Filler Preparation**

Ingots of the MPEA filler were cast by melting the pure constituents in a vacuum environment, and each ingot was melted twice to improve its bulk compositional homogeneity. Combustion-based carbon content analysis was conducted on the cast filler using a LECO CS344 analyzer. To produce foils 60  $\mu m$  thick, sections of the ingot with a 5 mm initial thickness were cold rolled to 400  $\mu m$  on a 4-inch diameter rolling mill, annealed under vacuum at 850°C for 2h, and subsequently cold rolled again to 60  $\mu m$  using a 2.5-inch diameter finishing mill. The boron-suppressed MBF80 and MBF91 foils were used in their as-received, melt-spun condition [20, 21] with a thickness of approximately 30  $\mu m$ .

#### **Brazing**

Pairs of rectangular prism coupons of IN738LC with dimensions  $6 \times 6 \times 12$  mm were brazed together and heat treated in a graphite hot zone vacuum furnace using the thermal history displayed in Fig. 1(a). Prior to brazing, base material faying surfaces were prepared to a 600-grit finish. The brazing step was performed at 1200°C for 90 min, followed by the industrially recommended dual-aging treatment for IN738LC, to re-precipitate a bimodal size distribution of  $\gamma$ ' in the base

material [2, 4]. Re-precipitation was necessary because the braze temperature is above the typical  $\gamma$ ' solvus. The dual-aging treatment is 2h at 1121°C (2050°F), followed by 24h at 843°C (1550°F). As depicted in Fig. 1(b), samples were brazed in an unfixed joint-clearance configuration using each of the three foils (MPEA, MBF80, MBF91). Because the thickness of the MBF80 and MBF91 foils was approximately half that of the MPEA, two foils were stacked on top of one another for the MBF80 and MBF91 brazes, to maintain the initial braze joint clearance consistently at 60  $\mu$ m for all samples.

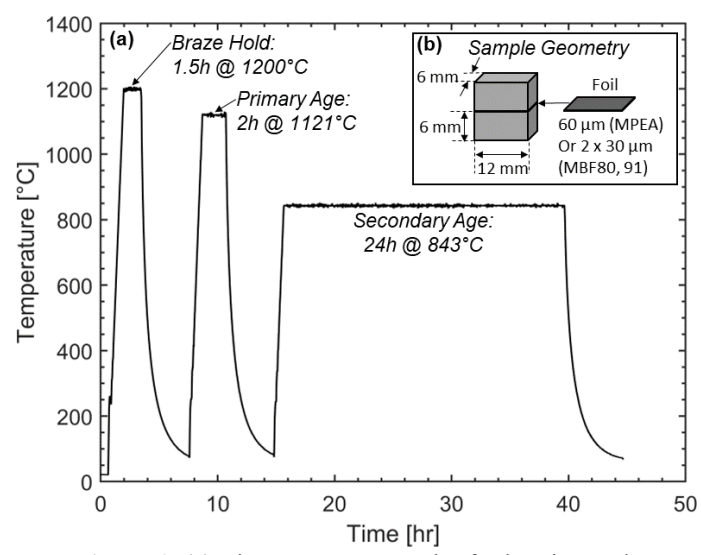


**Figure 1.** (a) Time-temperature plot for brazing and subsequent dual-age heat treatment for all samples. (b) Braze sample geometry.

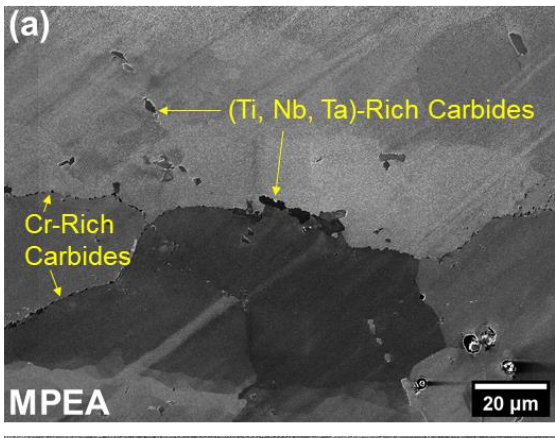
## Characterization

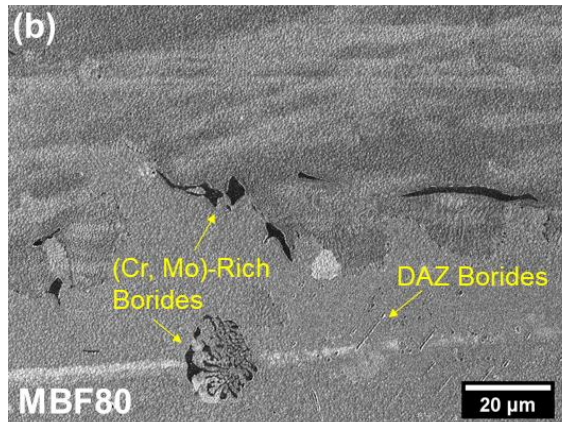
Following brazing and heat treatment, samples were bisected and then polished using standard metallographic procedures with a final step of 0.04 µm colloidal silica on a vibratory polisher for 12 to 18h, as preparation for microscopy and microhardness characterizations. Scanning electron microscopy (SEM) was performed using a Tescan S8252G SEM with an energy dispersive spectroscopy (EDS) detector. Accelerating voltage and beam current settings were 20kV/10nA for EDS and low magnification imaging, and 5kV/300pA for high magnification imaging. Microhardness was measured using a Vickers indenter tip. A load of 200gf, dwell time of 10s, and indent interspacing of 100 um were used. Indents were placed in a rectangular grid, with the grid set at an oblique angle of approximately 18.5° to the plane of the braze. This angular offset placed particular indents within the grid at the same distance from the braze centerline, allowing the hardness profile perpendicular to the centerline to be characterized at a spatial resolution of 31 µm, despite the 100 um indent interspacing. The oblique grid allowed statistics to be taken over four individual indents.

## **Results and Discussion**

#### **Distribution of Carbides and Borides**

Figure 2 displays a low magnification SEM image of each braze, highlighting secondary phases on the order of  $1-10 \mu m$ .





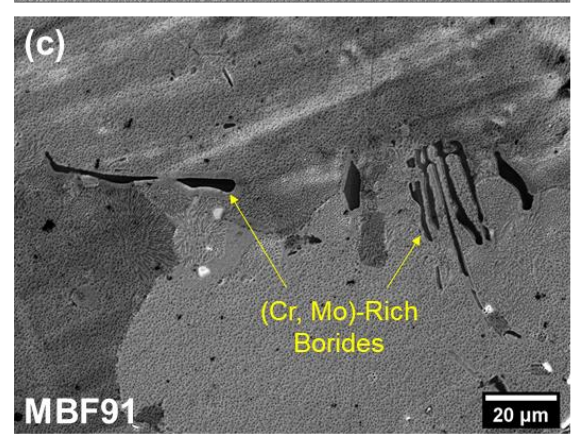


**Figure 2.** Low magnification SEM images highlighting the distribution of micron-scale secondary phases in (a) the MPEA braze, (b) the MBF80 braze, and (c) the MBF91 braze.

Figure 2(a) illustrates that the MPEA braze possesses a distinct centerline grain boundary that is substantially populated with secondary phases in this size range, as well as other, branching grain boundaries that are more variably decorated. Two distinct secondary phases are observed at the centerline grain boundary: a blockier phase typically around  $5-10~\mu m$  in size that is also observed sporadically throughout the intragranular space in both the braze and base material, and a smaller phase on the order of 1  $\mu m$  that occurs exclusively along grain boundaries. The EDS map overlay in Fig. 3 highlights the differences in Cr and Nb content of each phase. Along with previous synchrotron X-ray diffraction measurements [16, 22], Fig. 3 confirms that the blocky phase is a (Ti, Nb, Ta)-rich MC-type carbide, while the smaller grain boundary phase is a Cr-rich carbide that is

likely a M<sub>23</sub>C<sub>6</sub> stoichiometry. Because the filler carbon content analysis indicated negligible carbon (< 35 ppm) in the cast MPEA, the primary source of carbon to form these phases in the braze is the 0.11 wt.% nominal C content of the IN738LC base material [4]. Carbon, along with other elements specific to the base material, is incorporated into the molten filler by progressive dissolution of the base material resulting in filler dilution early in the brazing process [22].

The equilibrium transition temperatures of each carbide phase explain their distribution in the microstructure. Thermodynamic calculations show that the MC carbide has a melting point higher than the brazing temperature and does not dissolve before melting, and therefore floats in the braze filler while it is molten. Some, but not all, of the floating MC carbide particles become trapped in the intragranular space as the MPEA braze directionally solidifies from the base material toward the center, and the remaining particles get pushed all the way to the centerline as the MPEA solidification terminates there. In contrast, the Cr-rich carbides are only stable at lower temperatures, typically precipitating in IN738LC at service temperatures ranging from 760-980°C [23]. This phase should therefore be fully dissolved at both the brazing and primary age temperature, and nucleates and grows at grain boundaries exclusively during the secondary age hold at 843°C.

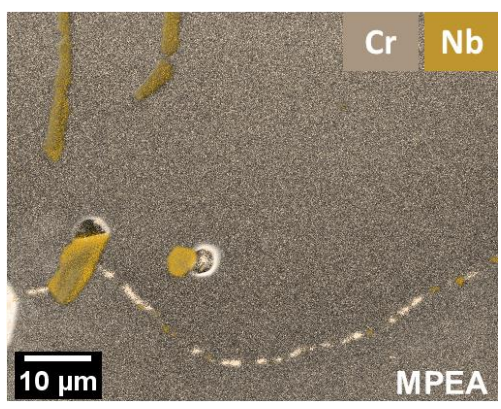


**Figure 3.** EDS map overlay of Cr and Nb from a region of the MPEA braze including the centerline grain boundary. The Nbrich particles are also enriched in Ti and Ta.

Figure 2(b) and 2(c) illustrate the MBF80 and MBF91 braze microstructures near the braze centerline. Both images display secondary phases, both in the intragranular space and at grain boundaries, that are (Cr, Mo)-rich borides. The EDS maps in Fig. 4(a-c), corresponding to the location of Fig. 2(c), confirm enrichment of Cr, Mo, and B in the secondary phases. Figure 4(d) also indicates that the boride phases reject Ti, causing local Ti enrichment in the surrounding material.

Examples of blocky standalone borides, as well as lamellar morphologies consistent with terminal eutectic solidification, are present in both Fig. 2(b) and Fig. 2(c). These images show that either morphology may exceed 20 µm in both the MBF80 and MBF91 braze. Figure 2(b) shows several smaller, aligned boride particles in the MBF80 braze microstructure, which could be representative of a diffusion affected zone (DAZ) [10, 24]. No such features are apparent in the MBF91 braze microstructure in Fig. 2(c).

The presence of athermally solidified borides in both the MBF80 and MBF91 brazes indicates that the 90-minute braze hold employed in the experiments is not sufficient to effectuate complete isothermal solidification. Some residual liquid remains in the braze seam and solidifies at the onset of cooling. This finding is consistent with literature studies, which reported substantially longer hold times on the order of 10 hours required when the joint clearance is 25 µm [8], which is less than half the clearance used in this study. Since the MPEA filler does not introduce borides or any other intermetallic phases, brazing with this filler is a possible means to avoid introducing embrittling microconstituents after a 90-minute hold. However, while both the Ti-rich and the Cr-rich carbides appear in the IN738LC base material following the dual-aging treatment, the decoration of grain boundaries is most significant near the MPEA braze centerline. A possible explanation for the greater number of grain boundary carbides in MPEA braze relative to the MBF80 and MBF91 brazes is that the absence of boride phases in the MPEA leaves a greater concentration of free Cr and C to form carbides in this braze, since the boride particles are Cr-rich and can also dissolve C [25], therefore binding these two elements. The temperature-dependent kinetics of grain boundary carbide precipitation are being studied, with initial experiments indicating that slight manipulation of the thermal history can substantially mitigate the extent of grain boundary decoration.

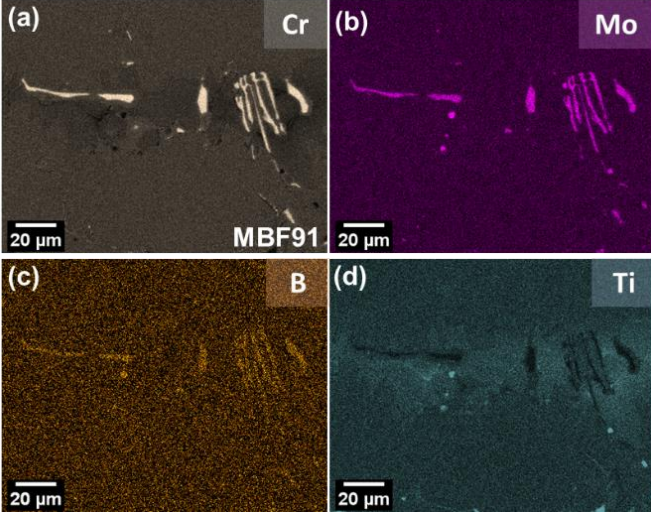


**Figure 4.** Individual EDS element maps of the MBF91 braze at the location corresponding to Fig. 2(c). (a) Cr, (b) Mo, (c) B, (d) Ti.

#### Distribution of $\gamma$ ' Precipitates

In addition to the impact of each brazing filler on the introduction and/or redistribution of larger boride and carbide phases, the effect of each braze on  $\gamma$ ' also carries critical implications for mechanical performance, as  $\gamma$ ' is the major strengthening phase in IN738LC. Figure 5 presents a collection of SEM micrographs illustrating the appearance of the  $\gamma$ ' precipitates in each braze as a function of distance from the braze centerline. Similar SEM images were analyzed by identifying the outline of each  $\gamma$ ' particle and measuring its area to quantify the total observed volume fraction of  $\gamma$ ' over this

range of distances from the centerline. At each distance, three individual images from the same cross section of the braze were analyzed. The quantified volume fraction data is displayed in Fig. 6. Together, Figs. 5 and 6 highlight key differences in the  $\gamma$ ' characteristics among brazes produced with the three foils.

In the MPEA braze, Figs. 5(a-d) illustrate that  $\gamma$ ' is present throughout the transverse profile. The presence of any  $\gamma$ ' at all near the braze center is noteworthy because the MnFeCoNiCutype MPEA used as the original brazing foil does not contain any Ti or Al, the main γ'-forming elements. This finding indicates that sufficient Ti and Al for y'-precipitation are introduced to the braze by a combination of dilution caused by progressive dissolution of the base material early in the braze process, and interdiffusion that occurs throughout the remainder of the braze hold, as well as during the dual-aging heat treatment. It also indicates that despite the local chemistry difference introduced by the disparate MPEA filler composition relative to IN738LC,  $\gamma$ ' is more stable than other intermetallics. Figure 6 shows that in the 35 µm nearest the braze center, the γ' volume fraction is approximately 26%-27%. By a centerline distance of 65 µm, however, the fraction rises to the 40%-45% range that is characteristic of the base material. Comparing Fig. 5(b) and 5(c) shows that, although locations at both an approximate centerline distance of 75 µm and 125 µm contain a  $\gamma$ ' volume fraction representative of the base material, the  $\gamma$ ' size distribution is still affected by the MPEA braze at the 75 μm mark. At 75 μm, the distribution is unimodal, and by 125 um, the distribution is bimodal, characteristic of dual-aged IN738LC, although the smaller secondary-γ' precipitates are not easily visible in Fig. 5(c).

For the MBF80 braze, Figs. 5(e-h), along with Fig. 6, show a relatively consistent presentation of  $\gamma$ ' precipitates across the transverse profile. Only in Fig. 5(e), near the immediate braze centerline, is the morphology of the  $\gamma$ ' affected, with the larger, primary-γ' precipitates displaying more oblong shapes, and the smaller, secondary-γ' appearing slightly larger than the secondary-γ' further into the base material. Figure 6 shows that the quantified volume fraction of  $\gamma$ ' is very consistent in the MBF80 braze, between 38% and 42% at all measured locations. Figures 5(i-l) show that like the MBF80 braze, the MBF91 braze microstructure displays appreciable differences from the  $\gamma$ ' characteristics typical of the base material only at the immediate braze centerline. However, in the case of the MBF91 braze, the differences are more significant. Figure 5(i) shows that the primary-γ' precipitates are enlarged and elongated, and there are few, if any, secondary- $\gamma$ ' precipitates in this image. Furthermore, Fig. 6 shows a substantial increase in the overall γ' volume fraction, to an average value of 56%, at the MBF91 braze centerline. The standard deviation is large, however, as the individual images analyzed presented volume fractions ranging from 44% to 64%. At centerline distances of 50 µm and greater, the MBF91 braze presents γ' volume fractions similar to those seen throughout the MBF80 braze, between 38% and 42%.

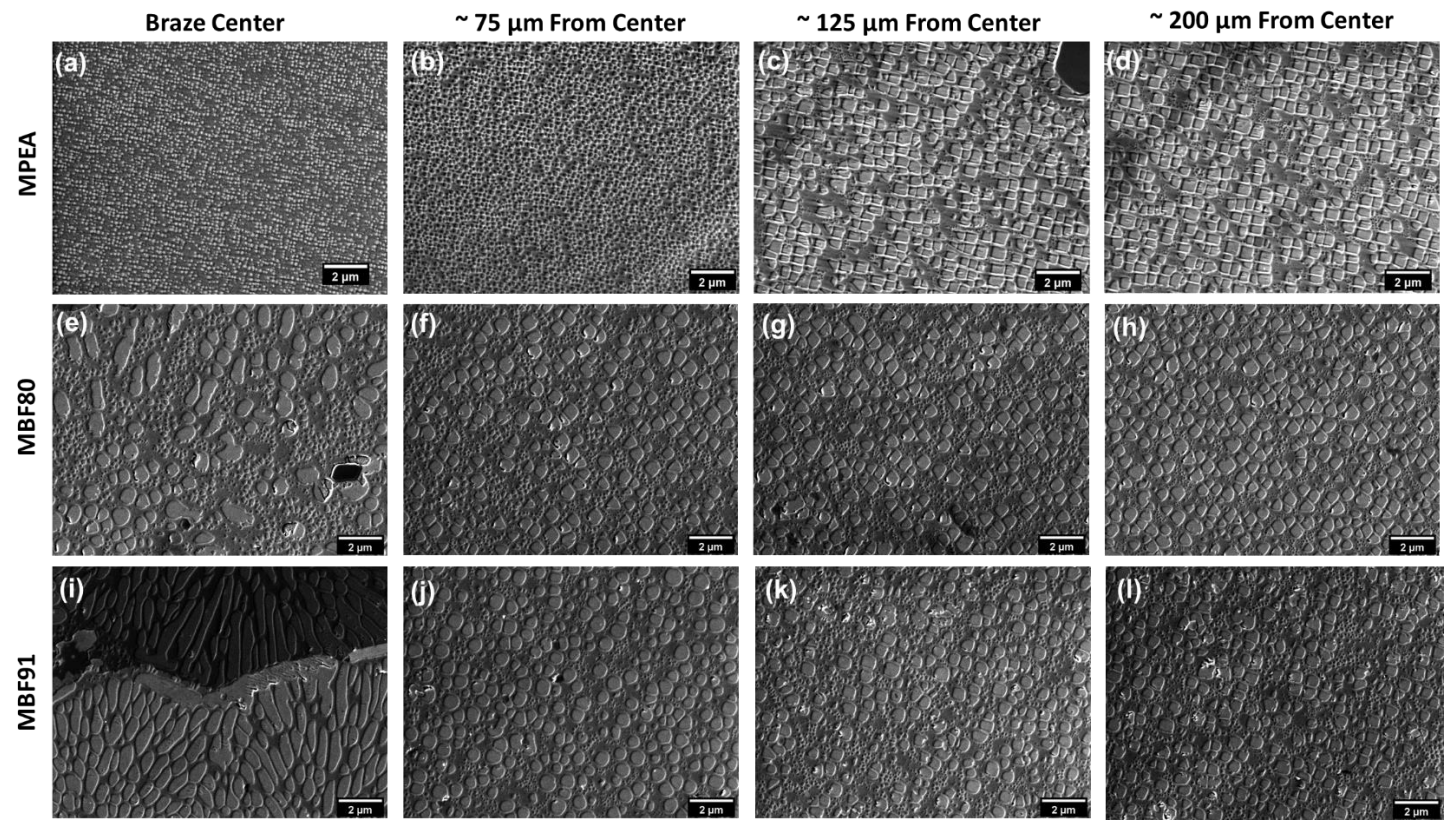


**Figure 5.** Collection of SEM images highlighting the appearance of the γ' precipitates in each braze, as a function of distance from the braze centerline. (a-d) MPEA braze. (e-h) MBF80 braze. (i-l) MBF91 braze.

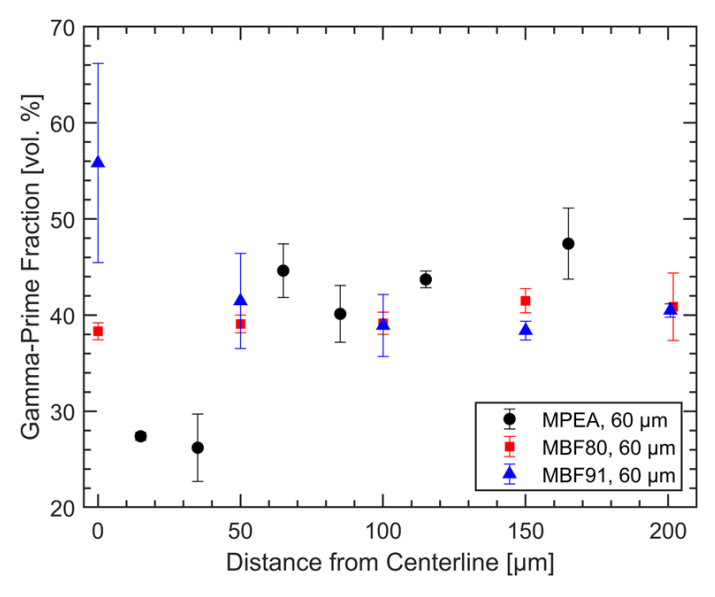
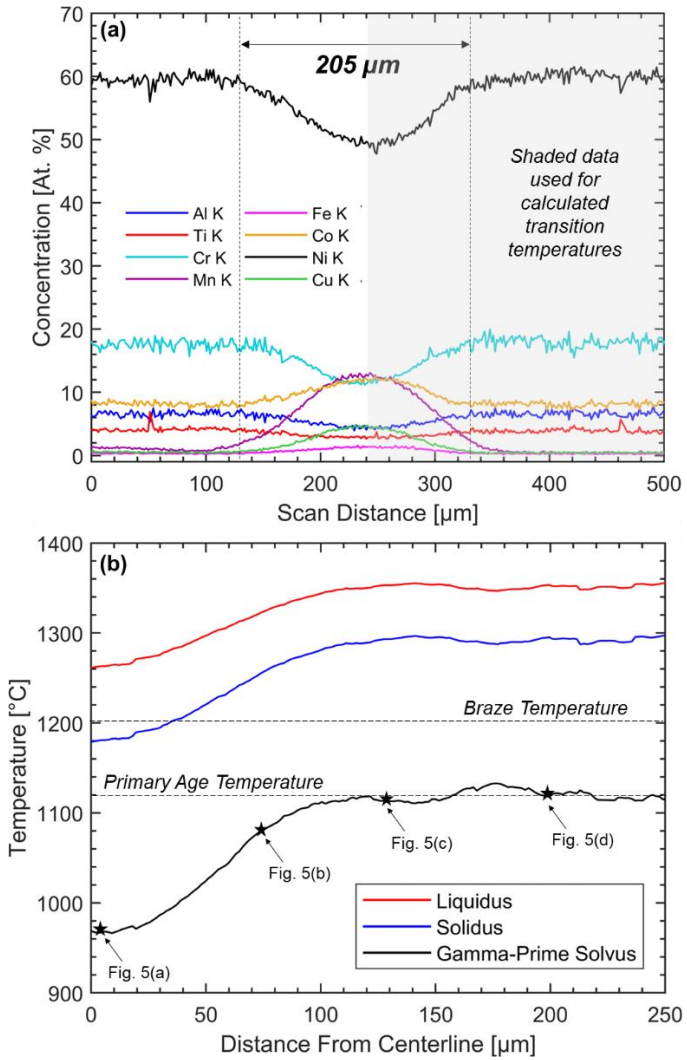


Figure 6. Quantified volume fraction of  $\gamma$ ' precipitates in each braze as a function of distance from the braze centerline, obtained from SEM image analysis. Error bars represent one standard deviation.

The data in Fig. 7 assist in explaining the observed  $\gamma$ ' behavior in the MPEA braze. Figure 7(a) displays the quantified EDS line-scan data across the MPEA braze transverse profile, with Nb, Mo, Ta, and W excluded for clarity. As indicated, the total width of the compositionally impacted zone is approximately 205  $\mu$ m. Considering that the original foil thickness was only

60 µm, this width is indicative of the extent of dilution and interdiffusion between the MPEA and the IN738LC base material. This width also indicates that compositional impacts on the  $\gamma$ ' behavior would be expected to extend out to about 100 µm from the braze centerline, which is consistent with the images in Fig. 5(a-d). The variation in the total amount of Ti and Al available to form  $\gamma$ ' can be gleaned from Fig. 7. While appreciable amounts of Ti and Al pervade the entire profile, these elements are somewhat more dilute near the braze center. Specifically, the average sum of the Ti and Al concentrations is measured at 10.5 at. % in the base material, and only 7.5 at. % within 35  $\mu$ m of the centerline. Considering the nominal  $\gamma$ ' stoichiometry of Ni<sub>3</sub>(Al, Ti) [2] and assuming that all the Ti and All is partitioned to the  $\gamma$ ' phase, these values translate to an expected molar fraction of  $\gamma$ ' of 41% in the base material and 30% at the braze center. When comparing these values to the observed volume fraction data in Fig. 6, relatively strong agreement is noted. A volume fraction of 41% is consistent with the unimpacted base material for all three brazes. The nearcenterline data for the MPEA of 26-27% are slightly lower than the value of 30% predicted from stoichiometry. This may be partially explained by the inherent difficulty in performing image analysis on the small precipitates exemplified in Fig. 5(a). It is also possible that the FCC-matrix near the center of the MPEA braze dissolves more Ti and Al than the matrix in the base material, allowing less to partition to  $\gamma$ ', which could be a signature of the high configurational entropy of the MPEA (e.g., [26]). It is noted that the molar fractions predicted by stoichiometry are not the same type of measurement as the volume fractions obtained from image analysis, but the differences in average atomic mass and density of the

disordered FCC and  $\gamma'$  phases are small and were therefore neglected when comparing the data.



**Figure 7.** (a) Quantified EDS composition profile for the MPEA braze excluding Nb, Mo, Ta, and W. (b) Calculated equilibrium transition temperatures using the EDS composition data, as a function of distance from the braze centerline.

The observed size distributions in Fig. 5(a-d) are explained by Fig. 7(b), which shows the transition temperatures calculated by the CALPHAD software Thermocalc using the TCNI11 database, over the range of input data shown in the shaded region of Fig. 7(a). A moving average spanning 15  $\mu m$  is applied to the data. The  $\gamma$ ' solvus temperature varies from about 965°C at the braze centerline to approximately 1120°C on average in the base material. Literature reports indicate the actual value of the  $\gamma$ ' solvus in IN738LC to be somewhat higher, ranging between 1120 - 1170°C, depending on local microsegregation [1].

The  $\gamma$ '-solvus profile is annotated with the locations of the images in Figs. 5(a-d), indicated as stars in Fig. 7(b). As shown, Fig. 5(c) and 5(d) are in the region where the  $\gamma$ ' solvus is at the base-material value. In this region, the 1121°C primary aging step is clearly just below the actual  $\gamma$ ' solvus, as precipitation of

the large primary  $\gamma'$  occurs during this heat treatment step. When the material is then reheated to 843°C, the γ-matrix is slightly supersaturated in Ti and Al at this lower temperature, resulting in the much slower precipitation of small, secondary- $\gamma$ ' in the space between primary- $\gamma$ ' precipitates. Hence, the full dual-age treatment results in the bimodal size distribution observed in Figs. 5(c) and 5(d), and throughout the microstructures of the MBF80 and MBF91 brazes. However, at the locations of Fig. 5(a) and 5(b), the  $\gamma$ ' solvus temperature is appreciably depressed, below 1121°C. Therefore, at these central locations of the MPEA braze,  $\gamma'$  remains in solution during the primary aging step and only precipitates during the 843°C secondary age, resulting in the unimodal size distribution observed in the figures. At the location of Fig. 5(b), the  $\gamma$ ' volume fraction is on par with the base material, but the compositional influence of the MPEA braze nonetheless depresses the  $\gamma$ ' solvus to be at least slightly below the primary aging temperature. It is noteworthy that the composition and transition temperature profiles in Fig. 7 would continue to evolve with exposure to elevated temperature during service of an IN738LC brazed component, trending toward homogeneity, resulting in increased  $\gamma$ ' volume fraction at the centerline over time.

Like the MPEA, the MBF80 or MBF91 fillers have no alloying additions of Al and Ti to the initial filler composition. However, the quantified EDS data for these elements in Fig. 8 indicate a relatively homogeneous concentration of Al and Ti in both the MBF80 and MBF91 brazes. As boron-suppressed brazing fillers with liquidus temperatures substantially below the brazing temperature [20, 21], both MBF80 and MBF91 induce progressive dissolution of the base material early in the brazing process [9], incorporating Al and Ti from the base material for  $\gamma^{\prime}$  formation. Without the slow-diffusing substitutional alloying additions of the MPEA to dilute the Ti and Al, their concentration is higher, and a larger volume fraction of  $\gamma^{\prime}$  precipitates near the centerline of the boron-suppressed brazes than the MPEA braze.

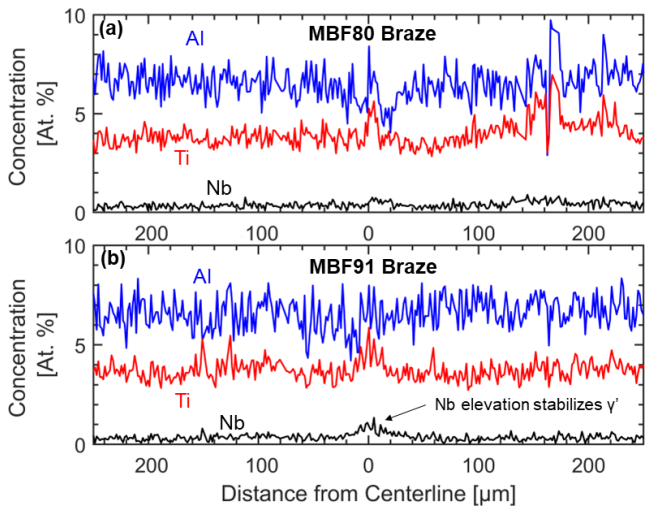


**Figure 8.** Concentration profile of Al, Ti, and Nb measured by EDS in (a) MBF80 braze and (b) MBF91 braze.

The difference in  $\gamma$ ' characteristics between the MBF80 and MBF91 brazes at the centerline is likely attributable to the

difference in Nb content between the two fillers. MBF91 contains a 4.0 wt. % Nb alloying addition that is absent in MBF80 [20, 21]. Note that the nominal Nb concentration of the IN738LC base material is only 0.9 wt. %. Smith and Patel discuss that adding Nb to a  $\gamma$ '-strengthened superalloy can increase the fraction of the  $\gamma$ ' phase and improve other important characteristics like the  $\gamma$ ' stability and flow strength [27]. As Nb is a slow-diffusing, substitutional element, the 4.0 wt. % Nb addition in MBF91 leads to an enduring local elevation of the Nb concentration near the centerline MBF91 braze following brazing and the dual-age heat treatment, which is confirmed by the elevation in the Nb concentration profile for the MBF91 braze observed in Figure 8(b). This, in turn, is responsible for the difference in the overall  $\gamma$ ' volume fraction observed between Fig. 5(e) and Fig. 5(i) and quantified in Fig. 6.

#### Effect of Phase Distribution on Microhardness

Figure 9 illustrates the effect of the constituent phase distribution on the Vickers microhardness profile of the brazes performed with each of the three foils. The figure shows that in each case, the microhardness is unaffected beyond 100  $\mu m$  from the braze centerline, averaging 400-410 HV in this region, characteristic of the base material. Approaching the centerline, the microhardness of the MPEA braze experiences a gradual, mild decrease to about 340 HV, attributable in part to the lower  $\gamma^{\prime}$  volume fraction in this region. The fact that the microhardness decrease is more gradual than the  $\gamma^{\prime}$  volume fraction decrease in Fig. 6 is possibly a signature of a degree of solid-solution hardening from the substitutional elements of the MPEA in the region  $\sim 30~\mu m$  from the braze centerline, which may offset some of the hardness decrease from the reduction in  $\gamma^{\prime}$ .

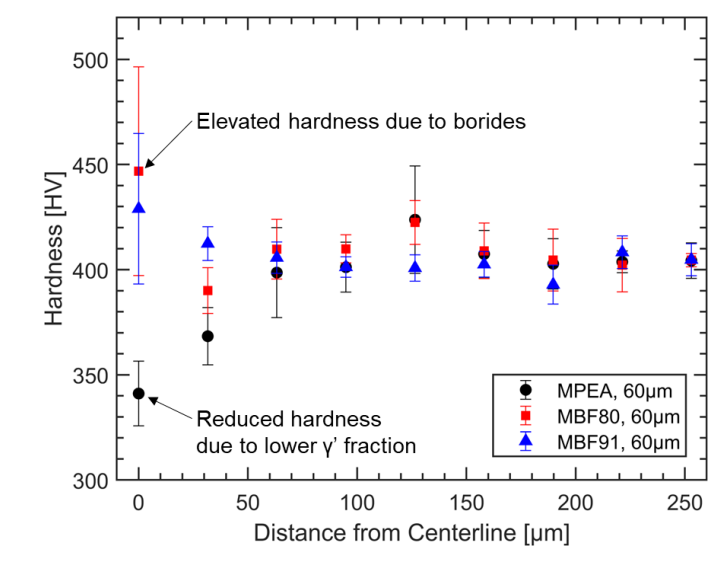


**Figure 9.** Vickers microhardness profiles as a function of distance from the braze centerline, for brazes performed using the MPEA, MBF80, and MBF91 foils. Error bars represent one standard deviation.

The MBF80 and MBF91 brazes exhibit hardness that remains similar to that of the base material, except for the set of indents placed at the immediate braze centerline. These indents exhibit average microhardness values of 430 HV for the MBF91 braze

and 450 HV for the MBF80 braze, with much wider standard deviations than those placed further from the centerline. The elevated averages are attributable to certain individual indents contacting the Cr-rich boride phase in these microstructures, which have high hardness and associated brittleness. The wider standard deviations result from averaging a mixture of high-hardness indents that contact borides, and other indents that did not contact borides with individual hardness characteristic of the base material. It is noteworthy that the 200gf load employed resulted in indents approximately 30 µm along the diagonal, which is larger than most of the borides exhibited in Fig. 2(b) and (c), so the hardness of the boride phase was never exclusively sampled. Using a smaller load or employing nanoindentation to sample the hardness of the boride phase in isolation would likely result in substantially higher values.

#### **Conclusions**

In comparing the observed phase distributions among the MPEA braze and the two boron-suppressed brazes of IN738LC subjected to the same thermal history, the following conclusions can be reached.

- The MPEA braze does not introduce any foreign/intermetallic phases to the microstructure after 90 minutes braze hold and the dual-age heat treatment, whereas both the MBF80 and MBF91 brazes introduce a Cr-rich boride.
- Both the MPEA and the boron-suppressed brazes form appreciable  $\gamma$ ' throughout the microstructure, using Al and Ti that is introduced from the IN738LC base material through progressive dissolution of the base material early in the braze process.
- The substitutional elements of the MPEA dilute the  $\gamma$ -forming elements near the center of this braze, reducing the sum of the Al and Ti concentrations from 10.5 at. % to 7.5 at. %. A commensurate decrease in the  $\gamma$ ' volume fraction is observed, along with the absence of a bimodal size distribution caused by local depression of the  $\gamma$ ' solvus temperature below 1121°C.
- The microhardness profiles of the three brazes display behavior consistent with the constituent phase distribution, with the reduced γ' volume fraction causing a mild hardness decrease near the centerline of the MPEA braze, and the boride phase elevating the average centerline hardness in the two boron-suppressed brazes.

## **Acknowledgments**

This research is supported by the National Science Foundation under Award No. 1847630 and Award No. 2208777. Use of the Tescan S8252G SEM was supported by the National Science Foundation Division of Materials Research Award No. 1828454. The authors greatly appreciate Will Coughlan at Metglas, Inc. for donating samples of MBF80 and MBF91 foils, as well as Jianping Gu and colleagues at PCC Structurals, Inc, for donating the Inconel 738LC base material. Additional thanks to Krishna Divakarla at Colorado School of Mines for assistance with SEM image analysis.

### References

- [1] Rosenthal, R. and West, R.D.F., "Continuous Gamma-Prime Precipitation in Directionally Solidified IN738LC Alloy", *Materials Science and Technology* Vol. 15 (1999) pp. 1387-1394.
- [2] Guzman, I. et al., "Particle Size of Gamma Prime as a Result of Vacuum Heat Treatment of INCONEL 738 Super Alloy," Journal of Materials Engineering and Performance (2012).
- [3] Haafkens, M.H, and Matthey, J.H.G., "A New Approach to the Weldability of Ni-Base As Cast and Powder Metallurgy Alloys," *Welding Journa, Vol.* 61, No. 11 (1982).
- [4] Alloy IN-738 Technical Data, The International Nickel Company.
- [5] C.Y. Su, C.C. P., W.B. C., W.C. Lih, Plasma Transferred Arc Repair Welding of the Nickel-Base Superalloy IN-738LC, 6 (1997) 619-627.
- [6] David, S. A. *et al.*, "Weldability and Microstructure Development in Ni-Base Superalloys," *Numerical Analysis of Weldability*, Graz, Austria, 1997.
- [7] Ojo, O *et al.*, "Contribution of constitutional liquation of gamma prime precipitate to weld HAZ cracking of cast Inconel 738 superalloy", *Scripta Materialia* Vol. 50, No. 5 (2004), pp. 641-646.
- [8] Huang, X. and Miglietti, W., "Wide Gap Braze Repair of Gas Turbine Blades and Vanes—A Review," *Journal of Engineering for Gas Turbines and Power* Vol. 134, No. 010801 (2012), pp. 1-17.
- [9] Gale, W.F. and Butts, D.A., "Overview: Transient Liquid Phase Bonding," *Science and Technology of Welding and Joining* Vol. 9, No. 4 (2004) pp. 283-300.
- [10] Gale, W. F., and Wallach, E. R. "Microstructural Development in Transient Liquid Phase Bonding," *Metallurgical Transactions A*, Vol. 22A (1991), pp. 2451-2457.
- [11] Tillmann, W. et al., "Development of High Entropy Alloys for Brazing Applications," Welding in the World, Vol. 64 (2020), pp. 201-208.
- [12] Hardwick, L. et al., "Development of a Novel Ni-Based Multi-principal Element Alloy Filler Metal, Using an Alternative Melting Point Depressant," Metallurgical and Materials Transactions A, Vol. 52A (2021), pp. 2534-2548.
- [13] Gao, M. *et al.*, "Microstructural Evolution and Mechanical Properties of Nickel-Base Superalloy Brazed Joints Using a MPCA Filler," *Metallurgical and Materials Transactions A*, Vol. 50 (2019), pp. 5117-5127.
- [14] Schneiderman, B. et al., "Ductile Braze Repairs for Ni-Base Superalloys using Novel MPEA Filler," Welding Journal, Vol. 101, No. 3 (2022) pp. 85s 95s.
- [15] Z. Yu, B. Schneiderman, and M. Gao, US Patent Application P295882.US.01 881024-236, 2022.
- [16] Schneiderman, B. *et al.*, "Synchrotron X-ray diffraction analysis of constituent phases in transition joint between nickel alloy 738LC and a MnFeCoNiCu alloy," *Materialia*, Vol. 32, No. 101911 (2023).
- [17] Jamaloei, A.D. et al., "Characterization of microstructure and mechanical properties of dissimilar TLP bonding

- between IN718/IN600 with BNi-2 interlayer," *Journal of Manufacturing Processes*, Vol. 29 (2017), pp. 447-457.
- [18] Sheng, N. *et al.*, "M3B2 and M5B3 Formation in Diffusion Affected Zone During Transient Liquid Phase Bonding Single Crystal Superalloys," *Metallurgical and Materials Transactions A*, Vol. 46A (2015), pp. 1670-1677.
- [19] Miglietti, W. and DuToit, M., "High Strength, Ductile Braze Repairs for Stationary Gas Turbine Components—Part I," *Journal of Engineering for Gas Turbines and Power*, Vol. 132, No. 082102 (2010) pp. 1-12.
- [20] High Performance Brazing Filler Metal Product Listing, Metglas Technical Data Sheet MBFPL062112 (2012).
- [21] High Performance Brazing Filler Metal MBF90 Series New Product Release, Metglas Technical Data Sheet MBFPL10 15 2015 (2015).
- [22] Schneiderman, B., "Constituent Phases and Their Stability in a Multi-Principal Element Alloy Filler for Brazing of Nickel-Base Superalloys", George S. Ansell Department of Metallurgical and Materials Engineering, Colorado School of Mines, 2022.
- [23] Kolagar, A. M. *et al.*, "Failure analysis of gas turbine first stage blade made of nickel based superalloy," *Case Studies in Engineering Failure Analysis*, Vol. 8 (2017), pp. 61-68.
- [24] Ojo, O. A. *et al.*, "Isothermal Solidification During Transient Liquid Phase Bonding of Inconel 738 Superalloy," *Science and Technology of Welding and Joining*, Vol. 9, No. 6 (2004), pp. 532-540.
- [25] Zhang, B. et al., "Precipitation and evolution of boride in diffusion affected zone of TLP joint of Mar-M247 superalloy," Journal of Alloys and Compounds, Vol. 695 (2017), pp. 3202-3210
- [26] Yeh, J. W. *et al.*, "Nanostructured high-entropy alloys with multiple principal elements: novel alloy design concepts and outcomes," *Advanced Engineering Materials*, Vol. 6, No. 5 (2004), pp. 299-303.
- [27] Smith G.D. and Patel, S. J., "The Role of Niobium in Wrought Precipitation-Hardened Nickel-Base Alloys," *Superalloys* 718, 625, 706 and Derivatives (2005) pp. 135-154.